1 **Plastic deformation of dry fine-grained olivine aggregates under high**

2 **pressures**

3

4 Reynold E. Silber[1,*,**], Jennifer Girard[1], Haiyan Chen[2] and Shun-ichiro Karato[1]

5

6 [1]Department of Earth and Planetary Sciences, Yale University, New Haven, 06511 CT, USA

7 [2]Mineral Physics Institute, Stony Brook University, Stony Brook 11794 NY, USA

8

9

10 *current address:

11 Northern New Mexico College (NNMC)

12 921 N Paseo De Onate, Española, NM 87532

13

14 **corresponding author (reynold.silber@gmail.com)

15

16

17

18 **ms# 9223R1**

19 Revision 2 submitted to American Mineralogist

20

21

22

23

24

25   **Abstract**

26   This study investigates the effect of pressure on diffusion creep of dry San Carlos and

27   synthetic (prepared by sol-gel method) olivine. We prepared dry (water content < 9 ppm wt)

28   fine-grained (< 1 μm grain-size) olivine and deformed the samples (both San Carlos and sol-

29   gel olivine in the same assembly) in the same sample assembly under high-pressure (P = 2.9–

30   8.8 GPa) and modest temperatures (T = 980–1250 K) at a fixed strain-rate. Evolution of

31   strength was studied using the radial X-ray diffraction from various diffraction planes. We

32   found that San Carlos and sol-gel olivine show similar rheological behaviour (when

33   normalized to the same grain-size). Stress estimated by the radial X-ray diffraction increases

34   with time and initially shows similar values for all diffraction planes. In many cases, stress

35   values start to depend on the diffraction planes in the later stage and time dependence

36   becomes minor. The micro-structural observations show that grain-size increases during an

37   experiment. The results are interpreted using a theory of radial X-ray diffraction and the

38   theoretical models of diffusion and dislocation creep. We conclude that the initial stage of

39   deformation is by diffusion creep, but deformation in the later stage is by dislocation creep.

40   For dislocation creep, our results are in reasonable agreement with previous low temperature

41   dislocation creep results after a correction of temperature effect. For diffusion creep, we

42   obtain an activation volume of 7.0 ± 2.4 cm^3/mol that is substantially smaller than the values

43   reported on dislocation creep but agrees well with the results on grain-growth. By comparing

44   the present results on dry olivine with the previous results on wet (water-saturated) olivine,

45   we found that water enhances diffusion creep but only modestly in comparison to dislocation

46   creep. The difference in the pressure and water content dependence between diffusion and

47   dislocation creep has an important influence on the dominant deformation mechanisms of

48   olivine in the upper mantle.

49

50

Introduction

52   Plastic deformation of minerals such as olivine occurs either by dislocation or diffusion

53   creep in most parts of the upper mantle (e.g., Karato et al., 1986; Karato and Wu, 1993; Hirth

54   and Kohlstedt, 1995a,b; Mei and Kohlstedt 2000a,b). Because some geophysically relevant

55   questions (e.g., seismic anisotropy, shear localization) are sensitive to deformation mechanisms,

56   it is important to explore the dominant deformation mechanisms in Earth's upper mantle and

57   understand how pressure might modulate it. The rate of deformation ($\dot{\varepsilon}$) is dependent on

58   pressure (*P*) and temperature (*T*) as

59
$$\dot{\varepsilon} = A \cdot \sigma^n \cdot d^{-m} \cdot exp\left(-\frac{E^* + PV^*}{RT}\right)$$
(1),

60   where *A* is a constant, *σ* is deviatoric stress, *d* is grain size, *R* is the gas constant, *E** is activation

61   energy, *V** is activation volume, *n* is the stress exponent and *m* is the grain size exponent and

62   both *n* and *m* depend on deformation mechanism (e.g., (Karato, 2008)).

63   Among the parameters in the flow law relation (Eq. (1)), *A, n, m* and *E** are relatively

64   easy to measure and reasonably well constrained for olivine for both diffusion and dislocation

65   creep at least under low-pressure conditions. In contrast, the activation volume (*V**) that

66   represents the pressure effects on deformation is difficult to measure, and most previous studies

67   on *V** were on dislocation creep (e.g., Dixon and Durham, 2018; Kawazoe et al., 2009; Li et al.,

68   2006). In the case of diffusion creep, not many studies were done to estimate *V** because of the

69   challenge in controlling grain size. In most previous studies on deformation in the deep upper

70   mantle, the activation volume of diffusion creep was assumed (e.g., Hirth and Kohlstedt, 2003;

71   Karato and Wu, 1993), and in such a case, the validity of such an assumption needs to be

72   evaluated. An exception is Mei and Kohlstedt (2000a), who reported *V**~15±5 cm³/mol based on

73   low-pressure data up to 0.45 GPa. However, the validity of their estimated uncertainties is

74   uncertain due to the low-pressure range used in their study. Among the reports based on the

75   higher pressure data, Nishihara et al. (2014) reported V^* of 8.2± 0.9 cm^3/mol for dry olivine in

76   the diffusion creep regime, using modestly small grain size samples based on the data from

77   P=3.0-5.4 GPa. However, under their experimental conditions, samples deformed in the mixed

78   regime and the estimated creep law parameters have large uncertainties. Another is Silber et al.

79   (2022) where they used natural San Carlos as well as synthetic fine-grained aggregates (~0.2-0.7

80   μm grain-size) and determined V^* of 2.5 ± 0.6 cm^3/mol for diffusion creep under the "wet"

81   (water-rich) conditions (P=3-10 GPa). In this paper, we report the activation volume of natural

82   and synthetic olivine samples made from San Carlos olivine or from sol-gel method, extending

83   the previous study (Silber et al., 2022) to "dry" conditions.

84   A key to this work is the preparation of fine-grained specimens, minimizing grain-growth

85   during deformation experiments, and the use of the *in-situ* radial X-ray diffraction with a help of

86   a theory (Karato, 2009) to infer the operating mechanisms of deformation. In the next section, we

87   describe the experimental procedure, including the sample preparation and characterization. And

88   in a later section, we summarize the experimental observations and present a flow law for

89   diffusion creep under dry conditions. In the final section we will discuss some implications of the

90   present results.

91

92   **Methods**

93   *Sample preparation*

4

94   To address potential difference in strength between San Carlos olivine ($Mg_{0.91}$,

95     $Fe_{0.09})_2SiO_4$, and synthetic olivine (solgel), two sets of samples were prepared. Following Karato

96   et al. (1986) we prepared fine-grained aggregates of San Carlos (SC) olivine. We selected

97   pristine San Carlos olivine crystals which were initially manually pulverized. Pulverized powder

98   was further ground in a ball mill for at least 24 hours. The ultrafine powder was extracted via

99   sedimentation technique. Separated ultrafine powder had an average grain-sizes between 100-

100   200 nm.

101   The ultrafine powder was then mixed with 1 wt% orthopyroxene (opx) to control the

102   silica activity. The grain growth mitigation was achieved by adding up to 5 wt% nano-size

103   (0.013 μm) alumina. The prepared mixture was baked at 1273 K in a controlled oxygen fugacity

104   gas furnace ($f_{O2} \sim 10^{-7}$ $^{-}10^{-8}$ (Pa)) and then loaded into the Ni capsule. These densely packed

105   samples were subsequently hot-pressed at 3 GPa and 1073 K for one hour.

106   The preparation of solution gelation (solgel) samples was done following the method

107   described by Faul and Jackson (2007). Specifically, dissolution of magnesium and iron nitrates

108   was caried out in ethanol and homogenized with tetraethyl orthosilicate. To remove ethanol from

109   the mixture, the solution was heated on a hot plate at 30° C for several days. During the heating,

110   the gelation was initiated by introducing small amount of nitric acid (HNO_3) to the solution

111   which was continuously stirred in a beaker with a magnetic agitator.

112   The final synthesis and drying of olivine with composition ($Fe_{0.1},Mg_{0.9},)_2SiO_4$ was done

113   by baking at high temperature (1273 K) under the oxygen fugacity using CO_2 and H_2 gas mixture

114   ($f_{O2} \sim 10^{-7}$-10^{-8} (Pa)). Finally, the synthesized crystalline material was milled again and sintered

115   as in the case of San Carlos olivine. Following this step, the samples of desired length and width

5

116 (1.3 × 1.0 mm) were core drilled and dried again under controlled f_{O2} to remove any water

117 absorbed from the environment.

118

Grain size, water content measurements and sample assembly

120   We measured the initial grain sizes of hot-pressed samples using a scanning electron

121 microscope (SEM) (FEI/Philips XL30 ESEM-FEG). As in our previous work, we encountered

122 difficulties in reliably measuring the grain size on polished and acid etched samples due to the

123 overall ultrafine grain size in our prepared polycrystalline aggregates where the grain boundaries

124 could not be resolved with desired clarity. To overcome that obstacle, grain size analysis was

125 performed on fractured sample surfaces (**Figure 1**) (the same technique was used by Silber et al.

126 (2022)). This approach was validated by simultaneously conducting the grain size analysis on

127 perfectly polished and acid etched samples and on the same, but fractured samples, originating

128 from a secondary olivine with substantially larger grain sizes (> 1 μm). The grain size

129 distribution was determined using the intercept method and multiplying the obtained values by

130 the conversion factor of 1.5 (e.g., Abrams, 1971; Cahn and Fullman, 1956) (**Figure 2**). Grain-

131 size was also measured from all samples after deformation experiments. The typical starting

132 grain size for solgel olivine was estimated to be in the range of ~0.15 - 0. 25 μm. In the case of

133 San Carlos olivine samples, the observed grain size was somewhat larger (~0.20 - 0.50 μm).

134   The water content was determined for representative samples to ensure that the water

135 content is small enough to observe "dry" behavior in plastic deformation. The measurement of

136 each representative sample set was conducted using Fourier Transform Infrared Spectroscopy

137 (FTIR) using Excalibur FTS 3000 with UMA 600 Microscope. For this analysis, representative

138 samples were sequentially finely polished. Polished samples were prepared to thickness of ~100

6

139   μm and scanned using 50 × 50 μm aperture. The collected spectra were analyzed between 3000

140   and 3700 cm^{-1}, corresponding to absorption bands generally associated with hydrogen in olivine.

141   The linear function was employed in background correction specifically for the purpose of

142   repeatability. The corrected and integrated infrared spectra was used to calculate hydroxyl

143   concentration Paterson (1982).

144   FTIR analysis of selected samples showed a small amount of water well below 9 ppm wt,

145   presumably acquired by samples during high-pressure experiments. After deformation, the

146   samples were analyzed again to confirm that water content did not change appreciably during the

147   deformation experiment (**Figure 3**).

148   The cell design and geometry followed the procedure established by Girard et al. (2020)

149   and used in Silber et al. (2022). In this arrangement, both San Carlos and solgel samples were

150   emplaced symmetrically relative to the center of the cell, separated by pyrope and platinum disc

151   strain markers. Therefore, the pressure and temperature (and the macroscopic stress) conditions

152   are nearly identical for these two samples.

153

154   ***Experimental procedure and uncertainty estimates***

155   In total, four deformation experiments were performed at the 6-BM B white X-ray

156   beamline at Advanced Photon Source (APS) in Argonne National Laboratory using a D-DIA

157   apparatus (e.g., Wang et al., 2003) (the experimental procedure is the same as in Silber et al.

158   (2022).

159   Prior to each deformation experiment in D-DIA, the X-ray beam calibration was

160   conducted while the sample assembly is under (nearly) hydrostatic condition. Diffraction data

7

161   was collected from the samples before uniaxial stress was applied and used as a reference in

162   order to calculate the differential stress during deformation (deviatoric stress during this stage

163   was kept minimum by retracting the differential rams). Also, pressure and temperature of each

164   run were estimated from the X-ray diffraction data on platinum and pyrope before deformation.

165   For equation of state (EOS) of platinum, we used the results reported by (Matsui et al., 2009; Zha

166   et al., 2008) and for pyrope (Hu et al., 2016; Zou et al., 2012; Fan et al., 2017).

167   The errors in pressure estimate result from the uncertainties of the molar volume of a

168   sample by X-ray diffraction and from temperature uncertainties in the equation of state including

169   thermal expansion. Consequently, we can take advantage of the fact that P-estimates from the

170   molar volume also depend on T and by using EOS's of two materials we can determine both P

171   and T. The uncertainties in the pressure estimate are ~ 0.5 GPa, and for temperature it is ~ 50 K.

172   In contrast to a case of dislocation creep, annealing was kept to a minimum to minimize

173   grain growth. The deformation, achieved by advancing vertically positioned opposite anvils at

174   uniform rate, was initiated 15 min after the target temperature was reached for each experiment

175   (time needed to collect high P-T spectra).

176   The collection of X-ray diffraction spectra during deformation experiments was

177   conducted in equal intervals (every 3 minutes). The strain of both San Carlos and solgel sample

178   was determined from the X-ray radiography images of strain markers, collected during the

179   deformation, between each X-ray diffraction.

180   The uncertainty in strain (and strain-rate) determined from the radiographic images in our

181   experiments ranges up to 10% and depends on the pixel size of the image relative to the sample

182   thickness, the quality of the image, processing software and total strain. Strain-rates were

183   between 0.2-9.5 x 10^{-6} s^{-1} (**Table 2**).

8

184   Stress was derived from the radial X-ray diffraction performed on each sample. This was

185   done at the same time intervals as strain data collection. The lattice strain, obtained from the

186   diffracted and azimuthally collected X-rays, was used in calculation of the differential stress σ_{hk}

187   for the particular (hkl) reflection in crystals during deformation. This approach is based on Singh

188   et al. (1998):

189     $$d_{hkl}(\psi) \propto d_{hkl}^0 \left\{ 1 + \frac{\sigma_u}{6M}(1 - 3cos^2\psi) \right\} \quad (2),$$

190   where d_{hkl} the d-spacing for the lattice plan (hkl) during deformation, d^0_{hkl} is the d-spacing under

191   the hydrostatic conditions for the lattice plan (hkl), M is the Voigt-Reuss-Hill average of shear

192   modulus, ψ is the azimuthal angle, and σ_u is the uniaxial stress applied on the material that we

193   want to estimate. Stress is estimated by fitting the d_{hkl} (ψ).

194   We used Plot85 in initial analysis (Dixon and Durham, 2018; Li et al., 2004; Li et al.,

195   2006; Vaughan et al., 2000). To determine stress in olivine, we used the best-observed

196   diffraction peaks obtained from (130), (131) and (112) planes. The errors in stress were

197   calculated using the same methodology as in Silber et al. (2022).

198

199   **Results**

200   *Microstructure and grain sizes*

201   **Figures 1 & 2** show the SEM images of representative samples, before and after

202   deformation experiments. The average initial and final grain sizes estimated from the intercepts

203   measurements are given in **Table 1**. Pressures, temperatures, and corresponding uncertainties for

204   each experiment are also shown in Table 1. We followed the methodology of grain size

205   quantification given by Silber et al. (2022). They showed that for samples with ultrafine grain

9

206 sizes (~0.1-1 μm), it is preferential to quantify the grain sizes from fractured surfaces. That is

207 clear from Figures 1 and 2, as this approach permits the sub-0.1 μm grains to be preserved and

208 quantified. A typical SEM preparation method using polishing and acid etching to expose grain

209 boundaries generally leads to obliteration of the smallest grains in etched samples and hence

210 would not be represented in general grain size distribution (i.e., **Figure 2**).

211   It can be seen from Figure 2 that appreciable grain growth occurred despite the

212 presence of OPX and pinning with nano-size alumina. However, the final grain sizes, in

213 experiments with the greatest grain growth, did not exceed 1 micron. Grain sizes in all samples

214 follow nearly log-normal distribution and grain boundaries exhibit typical ~120° angles.

215 ***Water content in the samples***

216   Although we did not add any water in our experiments, some water may come from the

217 sample assembly during high-pressure experiments (see e.g., Karato, 1989). Therefore, to

218 mitigate potential water diffusion from the cell assembly components, boron epoxy cube, boron

219 nitride sleeves, alumina pistons as well as sample were baked in the oven for 24 h prior to the

220 deformation experiments. We measured the water content of our sample before and after a

221 deformation experiment.

222   We estimated water content by FTIR. The representative FTIR spectra of initial and

223 recovered San Carlos olivine and solgel samples are shown in **Figure 3**. The observed initial

224 water content in samples hot-pressed at 3 GPa and subsequently dried under controlled fugacity,

225 is low (less than ~5 ppm wt) almost below the detectability limit. However, we observed higher

226 water content after deformation experiments < 9 ppm wt) which suggests some absorption of

227 water from the ambient air in the range of $3600 - 3400$ cm^{-1}. These values of water content are

228 less than the threshold water content to see "dry" behavior.

10

229   *Mechanical data*

230   The stress, calculated from X-ray diffraction peaks during the deformation experiments,

231   is plotted as a function of strain for each experiment for both San Carlos olivine and solgel

232   olivine samples (**Figure 4a-h**). All our experiments were deformed at a fixed strain rate to the

233   total strains of ~ 4 – 15% (Figure 4a-h).

234   In all experiments, we observed hardening in the initial stage. Also in this stage, the (hkl)

235   dependence of stress is negligible or very small. However, at a certain time (strain), (hkl)

236   dependence of stress becomes stronger. And after this stage where large (hkl) dependence is

237   observed, stress level becomes nearly independent of time (strain). Figure 4c,d is an exception,

238   where transition to nearly independent time-stress relationship is not observed due to the early

239   termination of the experimental run.

240   The figure also shows results for San Carlos olivine and sol-gel olivine. When grain-size

241   is similar, creep strength of these two olivine samples is similar, although strength is different for

242   different grain-size (see a discussion in the later section). The mechanical data also shows that

243   the stress level is sensitive to pressure. At higher pressures, stress (for a given temperature and

244   strain-rate) becomes larger.

245

246   **Discussion**

247   *Deformation mechanisms*

248   The flow law for high-temperature creep can generally be given by equation (1). For

249   diffusion creep, $n=1$ and $m=2$-3, whereas for dislocation creep $n=3$-5 and $m=0$ (Karato, 2008).

250   Therefore a common way to infer the operation of diffusion creep in an experimental study is to

11

251   determine *n* and *m* to show *n*=1 and *m*=2-3 (e.g., (Karato, 2008; Karato et al., 1986; Mei and

252   Kohlstedt, 2000a; Mei and Kohlstedt, 2000b)).

253   However, estimating these parameters under high-pressure deformation experiments is

254   challenging. Unlike low-pressure experiments (using the Paterson apparatus), a sample is

255   surrounded by several solid materials in the high-pressure deformation experiments (P>3 GPa)

256   (e.g., (Wang et al., 2003; Yamazaki and Karato, 2001)). Consequently, when strain-rate is

257   modified, various portions of a sample assembly are gradually deformed leading to a slow re-

258   distribution of stress/strain in a sample assembly. Therefore the strain-rate of a sample does not

259   change to a new strain-rate immediately, and this makes it difficult to determine the stress

260   exponent (a detailed analysis was made to estimate *n* for such a case is given by (Silber et al.,

261   2022)).

262   We use the following methods to infer the operation of diffusion creep following our

263   previous study (also see Silber et al., 2022): (i) a comparison of the strength of a polycrystalline

264   sample with the estimated strength of relatively coarse-grained specimens corresponding to

265   dislocation creep, (ii) a comparison of measured strength with strength calculated from a

266   theoretical model of diffusion creep and measured diffusion coefficients, (iii) the diffraction

267   plane (hkl) dependence of stress, and (iv) the analysis of time hardening using grain-growth

268   kinetics constrained by the initial and the final grain-sizes.

269   (i)   Let us take a case of SAN515 (initial grain-size ~0.2 micron, the final grain-size ~0.8

270   micron) where deformation experiment was conducted at P=5.9 GPa, T=1080 K and

271   strain-rate is 10^{-5} s^{-1}. The measured stresses in the initial parts of SAN515 (i.e., at 1 %

272   strain) is ~400 MPa that would correspond to a grain-size of ~0.3 μm. Based on the report

273   by (Kawazoe et al., 2009) on dry dislocation creep of olivine (~5 μm grain-size), we can

12

274   also calculate the stress of a sample at the same P, T and strain-rate if deformation were

275   by dislocation creep. The stress will be ~30-50 GPa (a large uncertainty is caused by the

276   (hkl) dependence of stress) at P=5.9 GPa, T=1080 K and strain-rate of 10^{-5} s^{-1} that is

277   much higher than the observed stress (~400 MPa). This large difference indicates that the

278   samples in our experiments deformed (at least initially) by grain-size sensitive (diffusion)

279   creep because of a much smaller grain-size (~0.3 micron) than grain-size in (Kawazoe et

280   al., 2009)'s samples (~5 μm).

281 (ii)   Using our mechanical results in Table 3, we calculated grain-boundary diffusion

282   coefficient δD for each experiment (assuming coble creep) and compared our estimates

283   with the Si and Mg grain-boundary diffusion coefficients in olivine reported in previous

284   studies (e.g., Fei et al., 2018; Fei et al., 2016). The diffusion coefficient calculated using

285   our creep data are well within one order of magnitude of the value estimated from

286   previous studies. We conclude that our results are in reasonable agreement with previous

287   reported diffusion coefficients (e.g., 2018; Fei et al., 2016).

288 (iii) A remarkable observation is that in most of the initial part of our experiments where

289   grain-size is small, the (hkl) dependence of stress is weak, whereas the (hkl) dependence

290   becomes large in the later stage where grain-size is larger (see Fig. 1). The (hkl)

291   dependence of stress provides an important clue on the deformation mechanism if one

292   uses a theory by (Karato, 2009). In a synchrotron deformation experiment, stress acting

293   on a sample is calculated from the lattice strain (equation (2)). As equation (2) indicates,

294   one can determine the lattice strain for different diffraction planes (hkl). The results often

295   show that stresses estimated for different (hkl) differ substantially (e.g., (Weidner et al.,

296   2004)). (Karato, 2009) showed that the (hkl) dependence of stress is caused mostly by

13

297   plastic anisotropy. And plastic anisotropy is strong for dislocation creep while it is weak

298   (or nearly zero) for diffusion (creep) (e.g., (Dohmen et al., 2002; Durham and Goetze,

299   1977; Houlier et al., 1990; Houlier et al., 1988; Jaoul et al., 1981)). Therefore, the

300   absence of (hkl) dependence (absence of plastic anisotropy) in the initial part of our

301   experiments is a strong indication of the operation of diffusion creep, and the gradual

302   transition to a marked (hkl) dependence in the later stage can be attributed to a transition

303   to dislocation creep by grain-growth.

304 (iv)   Those analyses strongly suggest that most of the initial stage of deformation is by grain-

305   size dependent diffusion creep. A complication is that because the strength in the

306   diffusion regime depends on grain-size that changes with time, the flow law must be

307   estimated based on the estimated grain-size at any point in the data. A simple way to

308   estimate grain-size during deformation is to interpolate the measured initial and final

309   grain-size assuming a relation for grain-growth (e.g., Chapter 13 of (Karato, 2008)),

310

311      $$d^{n_g}(t) - d^{n_g}(0) = kt \tag{3}$$

312

313 where d is grain-size, n_g is a grain-size exponent (=2-4 for most cases), t is time and k is a rate

314 constant that depends on temperature and pressure (and water content etc. (e.g., (Karato, 1989))).

315 Given the initial and the final grain-size, one can calculate k for a given condition (assuming a

316 few values of n_g), and consequently estimate the grain-size at any time during an experiment.

317 Therefore, one can determine the flow law corresponding to diffusion creep from the time-

318 dependent stress for a given run.

14

319   The values of k determined from the present study ($10^{-18\pm0.3}\,\mathrm{m^2 s^{-1}}$) are substantially lower

320   than the value extrapolated from Karato (1989) ($10^{-15.6}\,\mathrm{m^2 s^{-1}}$)). This is likely due to the pinning

321   effects by Al_2O_3. We also calculated K for ng=3 K=$10^{-22.7(+/-1.6)}\,\mathrm{m^3/s}$ and ng=4, K=$10^{-29.3(+/-1.6)}$

322   $\mathrm{m^4/s}$. Because grain-growth kinetics is so slow, different values of n_g do not make much

323   difference in estimated grain-size during deformation.

324   An issue in this approach is that, in most cases, the final stage of deformation occurs by

325   dislocation creep. In dislocation creep, grain-size could be controlled by the stress when dynamic

326   recrystallization is extensive (e.g., Karato et al., 1980). If this is the case, then the final grain-size

327   is not determined by grain-growth. To check this point, we compare the final grain-size from the

328   stress using the experimental data by van der Wal et al. (1993). We found that the grain-size

329   estimated from this relation is substantially smaller than the observed value suggesting that

330   dynamic recrystallization does not occur much. This is likely due to the low temperature, low

331   water content and small strain (for the temperature, water content and strain dependence of

332   dynamic recrystallization, see Zhang et al., 2000).

333

334   *Activation volume for diffusion creep*

335   We estimate activation volume for diffusion creep based on the data at different

336   pressures. We select data corresponding to diffusion creep based on the criteria discussed above.

337   However, since rheological behavior in diffusion creep also depends on grain-size (and

338   temperature), we need to compare the results at different pressures for the same grain-size and

339   temperature (normalization). We compare strain-rate at different pressures at a common stress

340   (50 MPa), a common grain-size (1 micron), and a common temperature (1100 K) using equation

341   (1) ($n = 1$) assuming $m = 2$ or 3. Also, in normalizing with respect to temperature, we used $E^* =$

15

342   295 or 375 kJ/mol, which represents the most common range of activation energy values in

343   published literature.

344   The experimental stress and strain-rate, along with calculated grain sizes, required for

345   normalization are given in **Table 2**. The values of stress and strain reported in Table 2 were

346   taken at a point on the stress/strain curve before diffusion creep terminated. The reasoning is

347   that rheological data (strain-rate, stress) for diffusion creep are evolving (because of concurrent

348   grain-growth). We chose the data within a regime where (hkl) dependence is nearly zero and

349   time-hardening is present. As we showed before, the data in that regime follows the creep law

350   (Eq. (1)), and therefore as far as the data follows that equation, choice of data does not affect our

351   analysis.

352   To calculate activation volume from our data, we need to compare data at different

353   pressures at a common stress, grain-size and temperature (T_0, d_0, σ_0, are the normalization

354   temperature ($T_0 = 1100$ K), normalization grain size ($d_0 = 1$ μm), normalization stress ($\sigma_0 = 50$

355   MPa)). Figure 6 shows plots of normalize strain-rate as a function of pressure.

356   We calculate the activation volume using the following relationship:

357

358        $$V^* = -RT \frac{\partial log\, \dot{\varepsilon}(T_o, d_0, \sigma_o)}{\partial P}$$ (4)

359

360   where $\dot{\varepsilon}(T_0, d_0, \sigma_0)$ is the normalized strain rate and T_0, d_0, σ_0 are the normalization temperature

361   ($T_0 = 1100$ K), normalization grain size ($d_0 = 1$ μm), normalization stress ($\sigma_0 = 50$ MPa),

362   respectively.

16

<

386   than the solidus, we do not expect any effects of partial melting which might have played role in

387   Faul and Jackson (2007) conclusions.

388

389   *A comparison with previous studies*

390   Our results on activation volume for diffusion creep are substantially smaller that the

391   values reported before by Mei and Kohlstedt (2000a) (15 ± 5 cm^3/mol) from low pressure

392   experiments ($P < 0.45$ GPa) and numerically derived estimates using a Markov chain Monte

393   Carlo (MCMC) based on low-pressure data (i.e., Jain and Korenaga, 2020; 24 ± 7 cm^3/mol). We

394   believe that the disagreement with previous experimental study (Mei and Kohlstedt, 2000)

395   indicates that the uncertainties in the estimated V* by (Mei and Kohlstedt, 2000) at a low

396   pressure range (0.1-0.45 GPa) are substantially larger than their estimate. Also a large

397   discrepancy between our results and Jain and Korenaga, 2020 is due to the fact that their

398   numerical calculations did not include data at high pressures. This comparison indicates the

399   importance of high pressure studies on plastic deformation.

400   The results of our present study are compared with those by Silber et al. (2022) for water-

401   saturated samples compared at the grain-size of 1 μm (m=3) and temperature of T=1100 K, stress

402   of 50 MPa (**Figure 6**). Water-saturated samples deform faster than samples from the present

403   study, and the pressure dependence is stronger for the samples from present than the water-

404   saturated samples reported by Silber et al. (2022). The activation volume from the current study

405   is 5.2 cm^3/mol as compared to V*=1.9 cm^3/mol from Silber et al. (2022). The difference in V*

406   between these two studies is partly due to the fact that in Silber et al. (2022) where samples were

407   saturated with water, water content in olivine changes with pressure because the water solubility

408   depends on pressure (e.g., Kohlstedt et al., 1996). In **Figure 6b**, we made a correction on the

18

409   pressure dependence of water content using the data by Kohlstedt et al. (1996). After this

410   correction, V* from Silber et al. (2022) is ~4 cm^3/mol that is somewhat smaller than the present

411   results on dry olivine.

412   Regarding the water effects, we use a flow law $\dot{\varepsilon} = A \cdot C_W^r \cdot \sigma^n \cdot d^{-m} \cdot exp\left(-\frac{E^*+PV^*}{RT}\right)$, and

413   use the results by Mei and Kohlstedt (2000) where they showed a correlation between "r" and

414   V*. V* is now determined to be ~7 cm3/mol, and from Mei-Kohlstedt (2000) we estimated r~0.8

415   that is substantially smaller than r for dislocation creep (r~1.2; Karato and Jung, 2003).

416   In Figure 7, we compare our data from this study with previously published dry diffusion

417   creep data obtained at low pressure (e.g., Karato,1986; Hirth and Kohlstedt, 1995; Mei and

418   Kohlstedt, 2000). After normalization the results agree within error bars. We also plotted wet

419   diffusion creep data and flow law by Silber et al., (2022) obtained at high pressure, and flow law

420   by Mei and Kohlstedt (2000) obtained at low pressure. After normalization those are also in good

421   agreement.

422   Nishihara et al. (2014) reported the results of deformation experiments of dry olivine

423   where they identified both diffusion and dislocation creep at pressures at 3.1 - 5.4 GPa and

424   temperature 1473 –1573 K yield activation volume of 8.2 ± 0.9 cm^3/mol and activation energy of

425   ~485 kJ/mol. Although the activation volume they reported agree well with our results, the

426   activation energy they estimated is much higher than those for diffusion and diffusion creep in

427   olivine (~200–400 kJ/mol; Andersson et al., 1989; Dohmen et al., 2002; Farver and Yund, 2000;

428   Farver et al., 1994; Gardés and Heinrich, 2011; Gérard and Jaoul, 1989; Jaoul et al., 1980;

429   Ryerson et al., 1989). We do not understand the cause for this discrepancy, but it is possible that

19

430   the discrepancy is caused by the operation of both diffusion and dislocation creep under their

431   experimental conditions.

432   On the other hand, there are some previous studies on diffusion in olivine single crystals

433   and aggregates. For example, Fei et al. (2016) conducted Si-diffusion experiments on iron-free

434   olivine aggregates and obtained the V^* of 4.0 ± 0.7 cm^3/mol and E^* of 220 ± 30 kJ/mol. Smaller

435   values of V* for forsterite (Fe/(Fe+Mg)=0) than San Carlos olivine (Fe/(Fe+Mg)=0.1) may be

436   the influence of Fe.

437   Our results on dislocation creep regime may be compared with the previously reported

438   results on the flow law of olivine aggregates in the dislocation creep regime under high-

439   pressures. When we compare our new results with the published results on the power-law

440   dislocation creep including (Dixon and Durham, 2018; Karato and Jung, 2003; Kawazoe et al.,

441   2009). In most previous studies cited above, deformation experiments were conducted at higher

442   temperatures than our present study. When these results are extrapolated to the P-T conditions

443   similar to ours, they predict substantially higher strength (stress) than we observed (e.g., using

444   Karato and Jung 2003 dry flow law we obtain stress of roughly 100GPa) (except for Dixon and

445   Durham (2018) where a low activation energy was assumed). This is likely due to the fact that

446   dislocation creep in our experiments likely occurred in the Peierls creep regime because of low

447   temperatures. Indeed a comparison with the results by (Mei et al., 2010) gives a better

448   agreement.

449

450   ***Implications for plastic deformation in the whole upper mantle***

451   As demonstrated before, important mechanisms of plastic deformation in most of the

452   upper mantle are either power-low dislocation creep or diffusion creep (e.g., (Karato and Wu,

453   1993)). The relative importance of these two mechanisms can be estimated if all the flow law

454   parameters (see equation (1)) are known. At the time when (Karato and Wu, 1993) was

455   published, V* for diffusion creep was not available and therefore they estimated V* based on the

456   experiments on diffusion-controlled dislocation recovery (Karato et al., 1993). Now with our

457   new data from this study as well as (Silber et al., 2022), we now have experimentally constrained

458   values of V* for diffusion creep for both water-saturated and dry conditions. In addition, we

459   have a new result on the water content sensitivity of diffusion creep.

460   Therefore, we now have a complete data set for dry olivine rheology for both dislocation

461   (Karato and Jung, 2003) and diffusion creep regime (this paper). The calculated deformation

462   mechanism maps are shown in **Figure 8** for 3, 12 GPa (at 1473 and 1673 K) for a range of water

463   content (0 (dry), 10, 100 and 1000 ppm wt). The parameters we used are listed in Table 3. For

464   simplicity, we assumed that m for diffusion creep is 3, n for dislocation creep is 3, and for

465   diffusion creep is 1. And we assume that strain-rate is constant and 10^{-15} s^{-1}.

466   We calculated strain-rates by these two mechanisms and determined the regime boundary

467   (**Figure 8**). Because V* differ between the two deformation mechanisms, the regime boundary

468   depends on pressure. Diffusion creep dominates over the power-law dislocation creep at

469   relatively high pressures. One caveat in this exercise is that we did not take into account of the

470   possible change in the rate-controlling slip system in the dislocation creep regime as suggested

471   by (Masuti et al., 2019).

472

473   **Acknowledgments**

481

482   **Data Availability**

483   All data required to replicate this study are uploaded to a freely accessible repository, Harvard

484   Dataverse, DOI: 10.7910/DVN/V98ETE (the dataset will be published upon acceptance of this

485   paper – the private link (NOT for distribution) to the data set is here:

486   https://dataverse.harvard.edu/privateurl.xhtml?token=dfc6afdf-1d6e-4025-b56c-93f4e869ba25).

487   Raw data were processed using Plot85, the open source software package developed by Stony

488   Brook (http://www.mpi.stonybrook.edu/NSLS/X17B2/Support/Plot85/plot85.htm). The strain

489   rates were measured from the time-stamped radiographic images using the open source software

490   JImage, available at https://imagej.nih.gov/ij/download.html, and the proprietary software

491   package Adobe Photoshop (www.adobe.com).

492   **References**

493   Abrams, H., 1971. Grain size measurement by the intercept method. Metallography 4, 59-78.

494   Andersson, K., Borchardt, G., Scherrer, S., Weber, S., 1989. Self-diffusion in Mg2SiO4
495   (forsterite) at high temperature. Fresenius' Zeitschrift für analytische Chemie 333, 383-
496   385.

497   Atkinson, H.V., 1988. Overview no. 65: Theories of normal grain growth in pure single phase
498   systems. Acta Metallurgica 36, 469-491.

499   Cahn, J.W., Fullman, R.L., 1956. on the use of lineal analysis for obtaining particle size
500   distribution functions in opaque samples. J. Metals, Medium: X; Size: Pages: 610-612.

501   Chakraborty, S., Farver, J.R., Yund, R.A., Rubie, D.C., 1994. Mg tracer diffusion in synthetic
502   forsterite and San Carlos olivine as a function of P, T and fO2. Phys Chem Miner 21,
503   489-500.

504   Chen, I.-W., and Argon, A.S. (1979) Grain boundary sliding and interphase boundary sliding in
505   power law creep. Acta Metallurgica, 27, 749-754.

506   Dixon, N.A., and Durham, W.B. (2018) Measurement of activation volume for creep of dry
507   olivine at upper-mantle conditoins. Journal of Geophysical Research, 123, 8459-8473.

508   Dohmen, R., Chakraborty, S. and Becker, H.-W. (2002) Si and O diffusion in olivine and
509   implications for characterizing plastic flow in the mantle. Geophysical Research Letters
510   29, 10.1029/2002GL015480.

511   Dohmen, R., Chakraborty, S., and Becker, H.-W. (2002) Si and O diffusion in olivine and
512   implications for characterizing plastic flow in the mantle. Geophysical Research Letters,
513   29, 10.1029/2002GL015480.

514   Durham, W.B., and Goetze, C. (1977) Plastic flow of oriented single crystals of olivine 1.
515   Mechanical data. Journal of Geophysical Research, 82, 5737-5353.

516   Fan, D., Lu, C., Xu, J., Yan, B., Yang, B., Chen, J., 2017. Effects of water on PVT equation of
517   state of pyrope. Physics of the Earth and Planetary Interiors 267, 9-18.

518   Farver, J.R., Yund, R.A., 2000. Silicon diffusion in forsterite aggregates: Implications for
519   diffusion accommodated creep. Geophysical Research Letters 27, 2337-2340.

520   Farver, J.R., Yund, R.A., Rubie, D.C., 1994. Magnesium grain boundary diffusion in forsterite
521   aggregates at 1000°–1300°C and 0.1 MPa to 10 GPa. Journal of Geophysical Research:
522   Solid Earth 99, 19809-19819.

523 Faul, U.H., Jackson, I., 2007. Diffusion creep of dry, melt-free olivine. Journal of Geophysical
524   Research: Solid Earth 112.

525 Fei, H., Hegoda, C., Yamazaki, D., Wiedenbeck, M., Yurimoto, H., Shcheka, S., Katsura, T.,
526   2012. High silicon self-diffusion coefficient in dry forsterite. Earth Planet Sc Lett 345-
527   348, 95-103.

528 Fei, H., Koizumi, S., Sakamoto, N., Hashiguchi, M., Yurimoto, H., Marquardt, K., Miyajima, N.,
529   Katsura, T., 2018. Pressure, temperature, water content, and oxygen fugacity dependence
530   of the Mg grain-boundary diffusion coefficient in forsterite. American Mineralogist 103,
531   1354-1361.

532 Fei, H., Wiedenbeck, M., Yamazaki, D. and Katsura, T. (2013) Small effect of water on upper-
533   mantle rheology based on silicon self-diffusion coefficients. Nature 498, 213-216.

534 Gardés, E., Heinrich, W., 2011. Growth of multilayered polycrystalline reaction rims in the
535   MgO–SiO2 system, part II: modelling. Contrib Mineral Petr 162, 37-49.

536 Gérard, O., Jaoul, O., 1989. Oxygen diffusion in San Carlos olivine. Journal of Geophysical
537   Research: Solid Earth 94, 4119-4128.

538 Girard, J., Silber, R.E., Mohiuddin, A., Chen, H., Karato, S.-i., 2020. Development of a Stress
539   Sensor for In-Situ High-Pressure Deformation Experiments Using Radial X-Ray
540   Diffraction. Minerals 10, 166.

541 Hansen, L.N., Zimmerman, M.E., Kohlstedt, D.L., 2012. The influence of microstructure on
542   deformation of olivine in the grain-boundary sliding regime. Journal of Geophysical
543   Research: Solid Earth 117.

544 Hirth, G. and Kohlstedt, D.L. (2003) Rheology of the upper mantle and the mantle wedge: a
545   view from the experimentalists, in: Eiler, J.E. (Ed.), Inside the Subduction Factory.
546   American Geophysical Union, Washington DC, pp. 83-105.

547 Hirth, G., Kohlstedt, D.L., 1995. Experimental constraints on the dynamics of the partially
548   molten upper mantle. Diffusion in the dislocation creep regime. J. Geophys. Res. 100,
549   15441-15449.

550 Houlier, B., Cheraghmakni, M. and Jaoul, O. (1990) Silicon diffusion in San Carlos olivine.
551   Physics of Earth and Planetary Interiors 62, 329-340.

552 Houlier, B., Jaoul, O., Abel, F., and Liebermann, R.C. (1988) Oxygen and silicon diffusion in
553   natural olivine at T=1300 0 C. Physics of Earth and Planetary Interiors, 50, 240-250.

24

554 Hu, Y., Wu, Z., Dera, P.K., Bina, C.R., 2016. Thermodynamic and elastic properties of pyrope at
555   high pressure and high temperature by first-principles calculations. Journal of
556   Geophysical Research: Solid Earth 121, 6462-6476.

557 Jain, C., Korenaga, J., 2020. Synergy of Experimental Rock Mechanics, Seismology, and
558   Geodynamics Reveals Still Elusive Upper Mantle Rheology. Journal of Geophysical
559   Research: Solid Earth 125, e2020JB019896.

560 Jaoul, O., Froidevaux, C., Durham, W.B., Michaut, M., 1980. Oxygen self-diffusion in forsterite:
561   Implications for the high-temperature creep mechanism. Earth Planet Sc Lett 47, 391-
562   397.

563 Jaoul, O., Poumellec, M., Froidevaux, C. and Havette, A. (1981) Silicon diffusion in forsterite: a
564   new constraint for understanding mantle deformation, in: Stacey, F.D., Paterson, M.S.,
565   Nicolas, A. (Eds.), Anelasticity in the Earth. American Geophsyical Union, Washington
566   DC, pp. 95-100.

567 Karato, S. (1989) Grain growth kinetics in olivine aggregates. Tectonophysics 155, 255-273.

568 Karato, S. (2008) Deformation of Earth Materials: Introduction to the Rheology of the Solid
569   Earth. Cambridge University Press, Cambridge.

570 Karato, S. (2009) Theory of lattice strain in a material undergoing plastic deformation: Basic
571   formulation and applications to a cubic crystal. Physical Review, B79,
572   10.1103/PhysRevB.79.214106.

573 Karato, S. and Wu, P. (1993) Rheology of the upper mantle: a synthesis. Science 260, 771-778.

574 Karato, S., and Jung, H. (2003) Effects of pressure on high-temperature dislocation creep in
575   olivine polycrystals. Philosophical Magazine, A., 83, 401-414.

576 Karato, S., Paterson, M.S. and Fitz Gerald, J.D. (1986) Rheology of synthetic olivine aggregates:
577   influence of grain-size and water. Journal of Geophysical Research 91, 8151-8176.

578 Karato, S., Rubie, D.C., and Yan, H. (1993) Dislocation recovery in olivine under deep upper
579   mantle conditions: Implications for creep and diffusion. Journal of Geophysical Research,
580   98, 9761-9768.

581 Kawazoe, T., Karato, S., Otsuka, K., Jing, Z. and Mookherjee, M. (2009) Shear deformation of
582   dry polycrystalline olivine under deep upper mantle conditions using a rotational
583   Drickamer apparatus (RDA). Physics of the Earth and Planetary Interiors 174, 128-137.

584 Kawazoe, T., Karato, S., Otsuka, K., Jing, Z., and Mookherjee, M. (2009) Shear deformation of
585   dry polycrystalline olivine under deep upper mantle conditions using a rotational
586   Drickamer apparatus (RDA). Physics of the Earth and Planetary Interiors, 174, 128-137.

25

587   Kohlstedt, D.L., Goetze, C., 1974. Low-stress high -temperature creep in olivine single crystals.
588   Journal of Geophysical Research 79, 2045-2051.

589   Li, L., Weidner, D.J., Chen, J., Vaughan, M., 2004. Stress measurements of deforming olivine ay
590   high pressure. Phys Earth Planet In 143-144, 357-367.

591   Li, L., Weidner, D.J., Raterron, P., Chen, J., Vaughan, M.T., Mei, S., Durham, W.B., 2006.
592   Deformation of olivine at mantle pressure using the D-DIA. European Journal of
593   Mineralogy 18, 7-19.

594   Masuti, S., Karato, S., Girard, J. and Barbot, S. (2019) Anisotropic plasticity of olivine single
595   crystals under wet conditions under the deep upper mantle conditions. Physics of the
596   Earth and Planetary Interiors 290, 1-9.

597   Matsui, M., Ito, E., Katsura, T., Yamazaki, D., Yoshino, T., Yokoyama, A., Funakoshi, K.-i.,
598   2009. The temperature-pressure-volume equation of state of platinum. J Appl Phys 105,
599   013505.

600   Mei, S. and Kohlstedt, D.L. (2000b) Influence of water on plastic deformation of olivine
601   aggregates, 2. Dislocation creep regime. Journal of Geophysical Research 105, 21471-
602   21481.

603   Mei, S., and Kohlstedt, D.L. (2000a) Influence of water on plastic deformation of olivine
604   aggregates, 1. Diffusion creep regime. Journal of Geophysical Research, 105, 21457-
605   21469.

606   Mei, S., Suzuki, A.M., Kohlstedt, D.L., Dixon, N.A., and Durham, W.B. (2010) Experimental
607   constraints on the strength of the lithospheric mantle. Journal of Geophysical Research,
608   115, 10.1029/2009JB006873.

609   Misener, D.J., 1974. , Cationic diffusion in olivine to 1400°C and 35 kbar, , Carnegie Inst. of
610   Washington, Washington, D.C.

611   Mohiuddin, A., Karato, S.-i., Girard, J., 2020. Slab weakening during the olivine to ringwoodite
612   transition in the mantle. Nature Geoscience 13, 170-174.

613   Nishihara, Y., Maruyama, G., Nishi, M., 2016. Growth kinetics of forsterite reaction rims at
614   high-pressure. Phys Earth Planet In 257, 220-229.

615   Nishihara, Y., Ohuchi, T., Kawazoe, T., Spengler, D., Tasaka, M., Kikegawa, T., Suzuki, A.,
616   Ohtani, E., 2014. Rheology of fine-grained forsterite aggregate at deep upper mantle
617   conditions. Journal of Geophysical Research: Solid Earth 119, 253-273.

618   Paterson, M.S., 1982. The determination of hydroxyl by infrared absorption in quartz, silicates
619   glasses and similar materials. Bulletin de minéralogie 105, 20-29.

620   Ryerson, F.J., Durham, W.B., Cherniak, D.J., Lanford, W.A., 1989. Oxygen diffusion in olivine:
621   Effect of oxygen fugacity and implications for creep. Journal of Geophysical Research:
622   Solid Earth 94, 4105-4118.

623   Silber, R.E., Girard, J., and Karato, S. (2022) Effects of pressure on diffusion creep in wet
624   olivine aggregate. Physics of the Earth and Planetary Interiors, 324, 106840.

625   Van der Wal, D., Chopra, P., Drury, M., and Gerald, J.F. (1993) Relationships between
626   dynamically recrystallized grain size and deformation conditions in experimentally
627   deformed olivine rocks. Geophysical Research Letters, 20(14), 1479-1482.

628   Vaughan, M., Chen, J., Li, L., Weidner, D., Li, B., 2000. Use of X-ray imaging techniques at
629   high-pressure and temperature for strain measurements. In: Manghnani, M.H., Nellis,
630   W.J., Nicol, M.F. (Eds.), AIRAPT-17. Universities Press, Hyderabad, India, 1097-1098.

631   Wang, Y., Durham, W.B., Getting, I.C., and Weidner, D.J. (2003) The deformation-DIA: A new
632   apparatus for high temperature triaxial deformation to pressures up to 15 GPa. Review of
633   Scientific Instruments, 74, 3002-3011.

634   Weidner, D.J., Li, L., Davis, M. and Chen, J. (2004) Effect of plasticity on elastic modulus
635   measurements. Geophysical Research Letters 31, 10.1029/2003GL019090.

636   Yamazaki, D. and Karato, S. (2001) High pressure rotational deformation apparatus to 15 GPa.
637   Review of Scientific Instruments 72, 4207-4211.

638   Zha, C.-S., Mibe, K., Bassett, W.A., Tschauner, O., Mao, H.-K., Hemley, R.J., 2008. P-V-T
639   equation of state of platinum to 80 GPa and 1900 K from internal resistive heating/x-ray
640   diffraction measurements. Journal of Applied Physics 103, 054908.

641   Zhang, Z., Karato, S.-I., 2021. The Effect of Pressure on Grain-Growth Kinetics in Olivine
642   Aggregates With Some Geophysical Applications. Journal of Geophysical Research:
643   Solid Earth 126, e2020JB020886.

644   Zou, Y., Gréaux, S., Irifune, T., Whitaker, M.L., Shinmei, T., Higo, Y., 2012. Thermal equation
645   of state of Mg 3 Al 2 Si 3 O 12 pyrope garnet up to 19 GPa and 1,700 K. Physics and
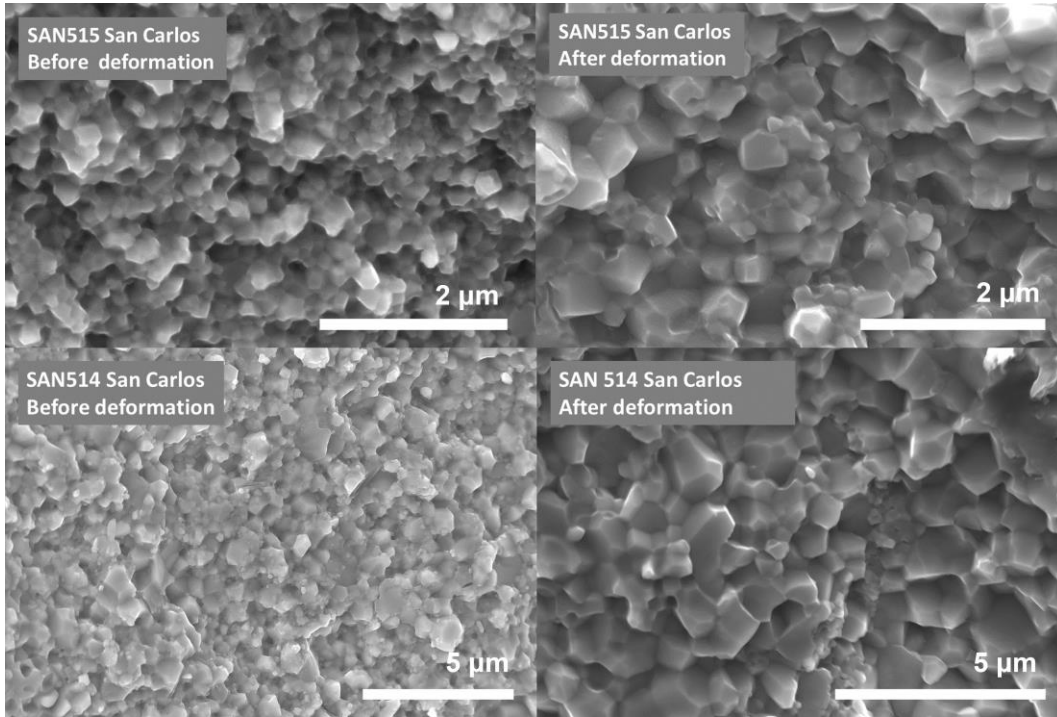646   Chemistry of Minerals 39, 589-598.

647

648

649

650

651

652 **List of Figures**

653 **Figure 1**: Example of microstructure (grain size) observed in initial samples (left) and the post-
654 deformation recovered samples. The scale bar in all images is in microns (μm).

655

656
657
658
659

28

660 **Figure 2:** Distribution of the grain sizes from different aggregates of San Carlos parent samples
661 (blue) compared with the grain size distribution after the deformation experiments (orange) at
662 given pressure and temperature conditions. The number of measured individual grain intercepts
663 (from multiple SEM images of the same sample) is given in each figure.
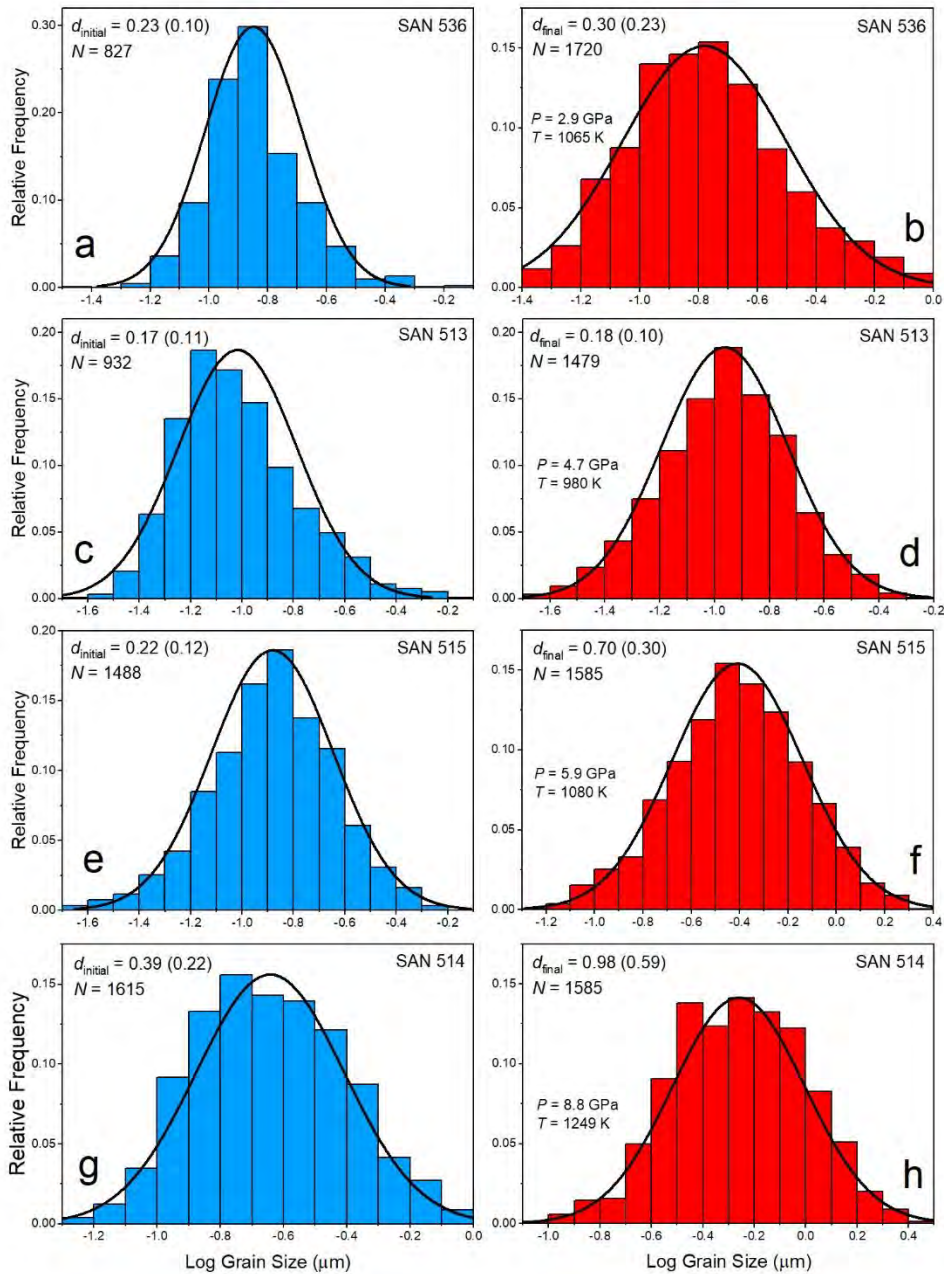
664

665

666   **Figure 3:** The representative FTIR of the of San Carlos olivine (top three panels) and
667   solgel (the bottom panel) samples before and after deformation.
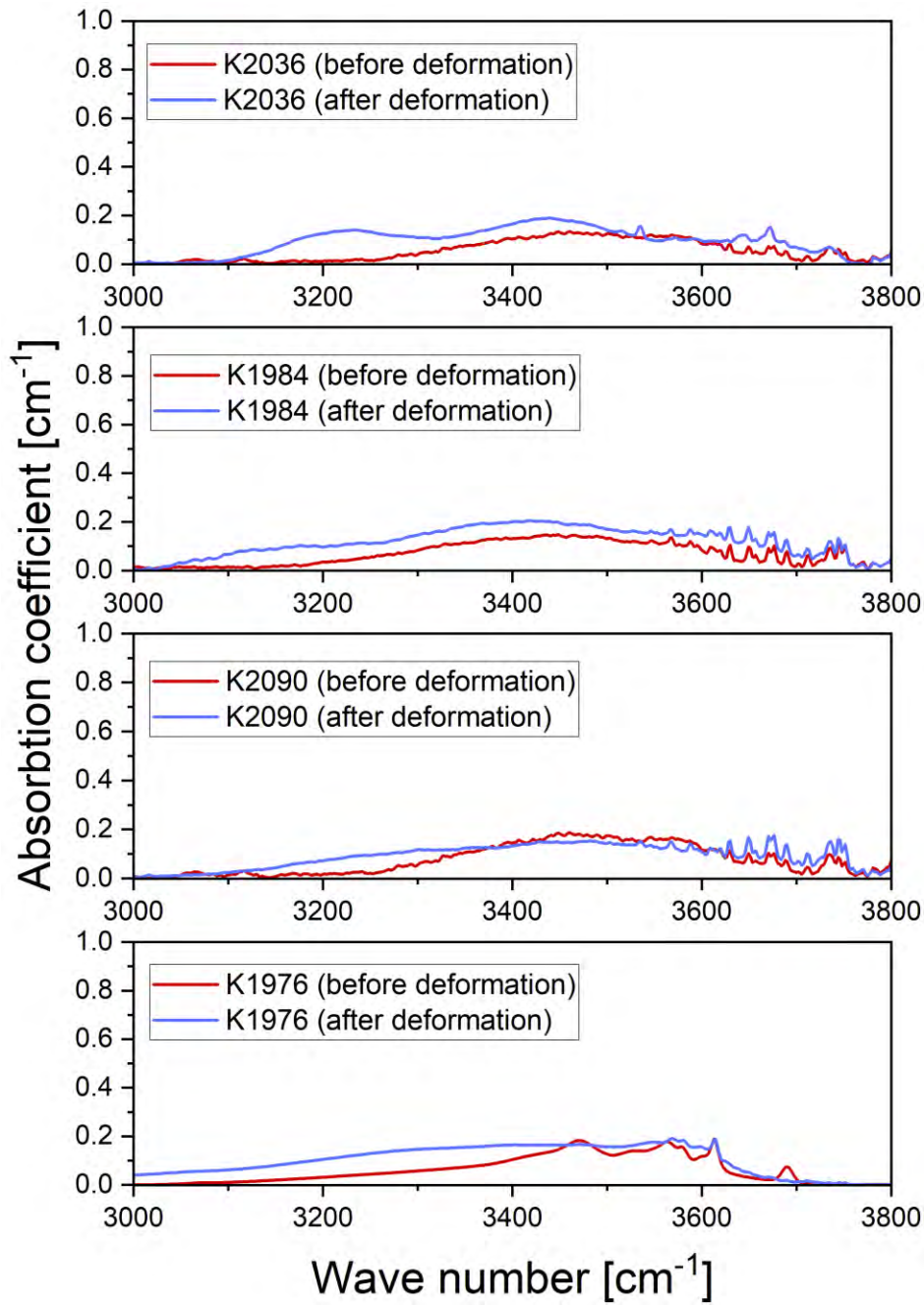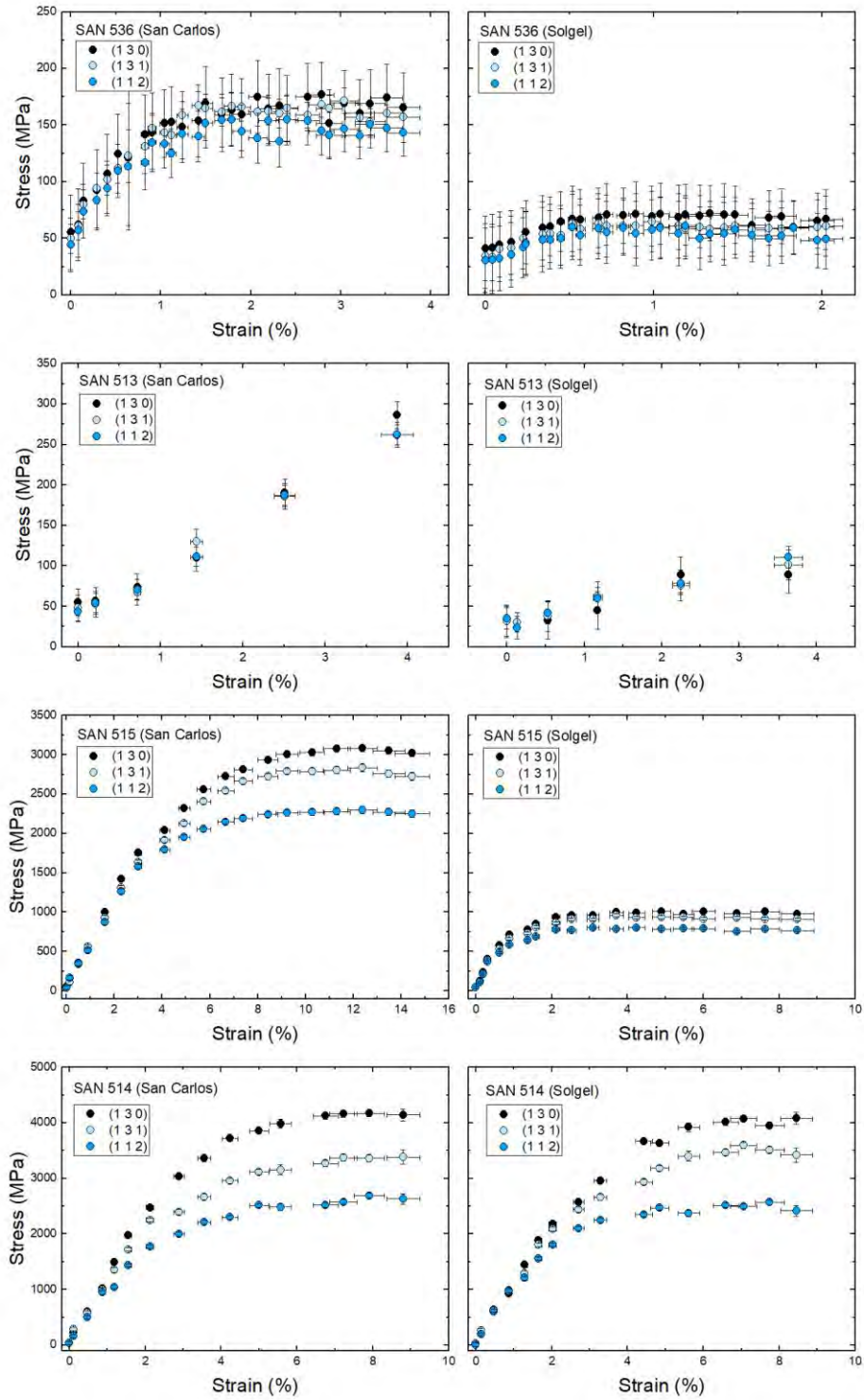

668

669

670

671   **Figure 4:** Differential stress vs. strain for all deformation experiments. For clarity, San Carlos

672   (left panels) and solgel (right panels) are plotted separately.

673

674 **Figure 5:** Example of linear regression analysis using our data, to obtain the activation volume

675 (V^*). Prior to the regression, data were normalized to a common temperature ($T = 1100$ K) using

676 activation energy of 295 kJ/mol and 375 kJ/mol, and common grain size ($d = 1$ μm) using grain

677 size exponents ($m = 2$ and 3). Data was also normalized to a common stress of 50 MPa using

678 stress exponent $n = 1$.
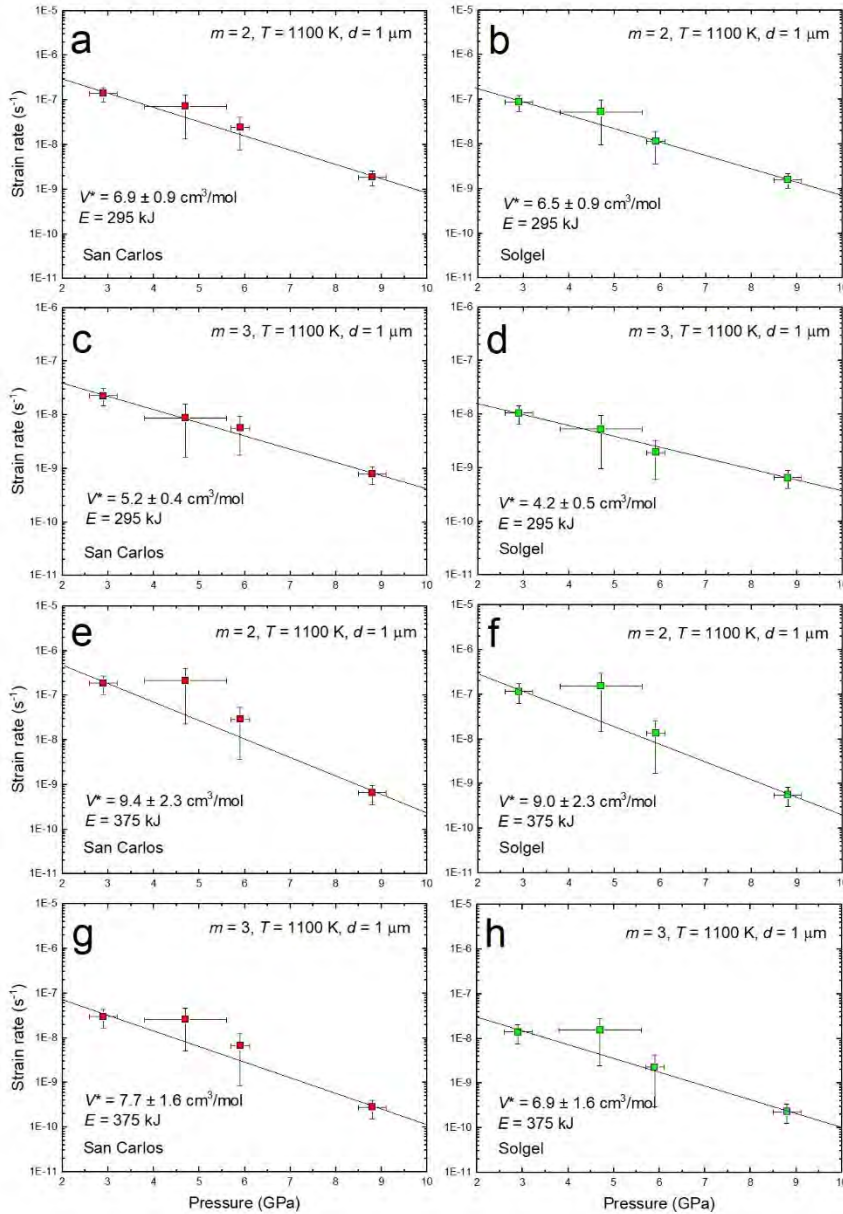
679

680

681 **Figure 6:** Comparison between mechanical strength of water saturated olivine samples (Silber et
682 al., 2022) and dry olivine samples at range of different pressures (normalized using
683 E*=295kJ/mol, S=50 MPa, T=1100 K, d=1 μm and m=3) a) comparison between Silber et al
684 (2022) under saturated conditions without correcting for water concentration increasing with
685 pressure, b) after applying the correction to Silber et al (2022) to account for the increase of
686 water solubility with depth.

687
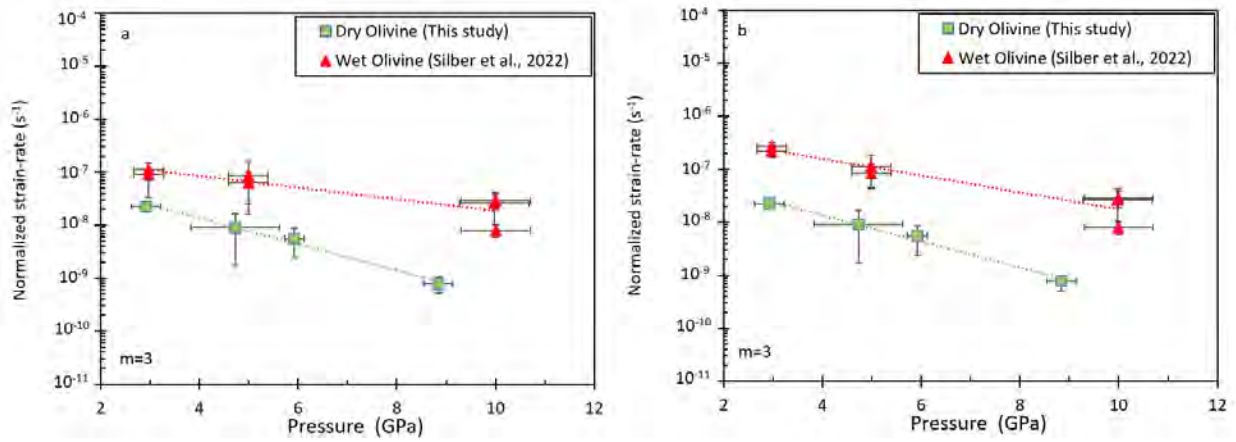
688
689
690
691
692
693
694
695
696
697
698
699
700

701 **Figure 7:** Comparison between "dry" and "wet" rheologies:

702 Strain-rates, obtained experimentally have been normalized to the same stress (100 MPa),

703 temperature (1100 K) with E* = 295kJ/mol, grain size (1micron) with m = 3, and pressure effect

704 have been removed to only see the effect of water (C_{OH}) on the rheology. Data reported in this

705 study are shown by the red square symbols. The rheological law obtained after our linear

706 regression is shown in green dashline. Data from Silber et al., (2022) are shown by the blue

707 square symbols and blue solid line. For comparison we also report Mei and Kohlstedt (2000) wet

708 diffusion creep rheology (black solid line) assuming r=0.75 and V*=5cm^3/mol. Additional data

709 are plotted for comparison, Mei and Kohlstedt (2000) dry data (black symbol), Karato et al.,

710 (1986) dry data (red symbol) and Hirth and Kohlstedt (1995) samples with melt fraction <0.01

711 (purple symbol). The green shaded region represents water detectability limit of our FTIR

712 measurements.
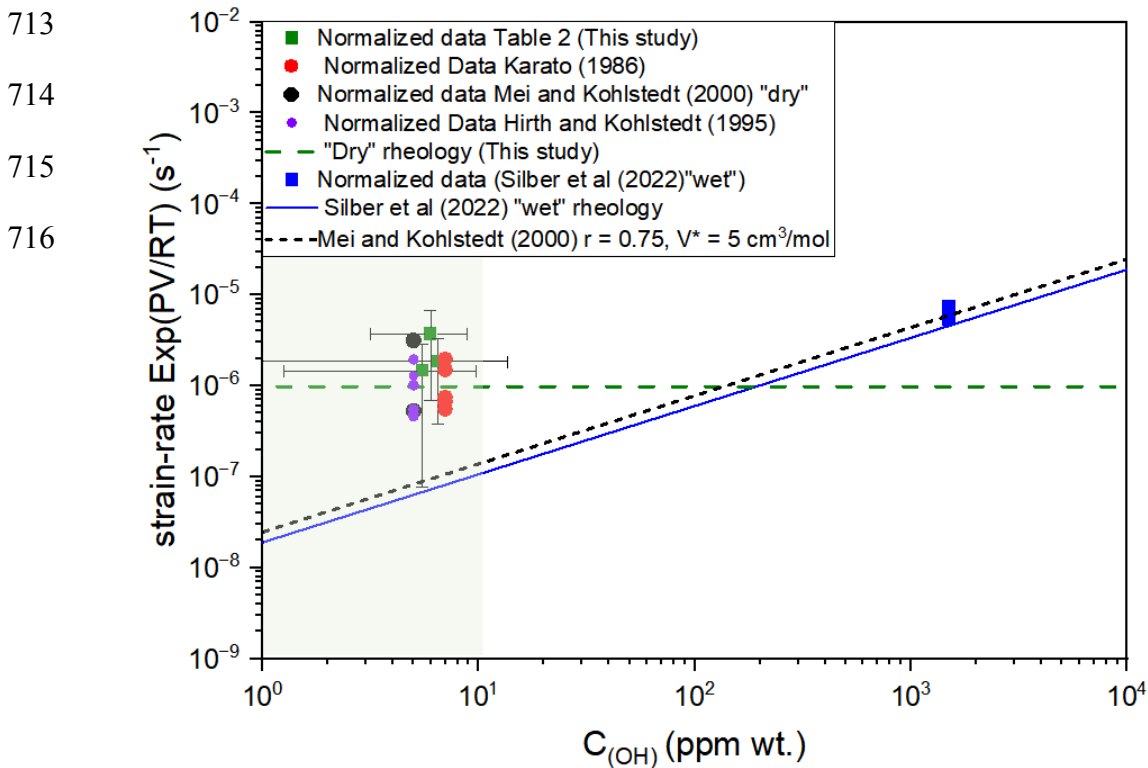
717 **Figure 8:** olivine deformation map under upper mantle pressure:

718 Stress versus grain size deformation map. The limit between diffusion and dislocation creep was

719 calculated at T=1473K as well as 1673K and at pressure of 3GPa(left) and 12GPa (right), for

720 m=3 (blue). The boundary between diffusion creep and dislocation creep region is represented by

721 different shades of blue for different water content from "dry" (light blue) to 1000 ppm wt H2O

722 (dark blue). The light blue region represents the range of grain size expected in the upper mantle

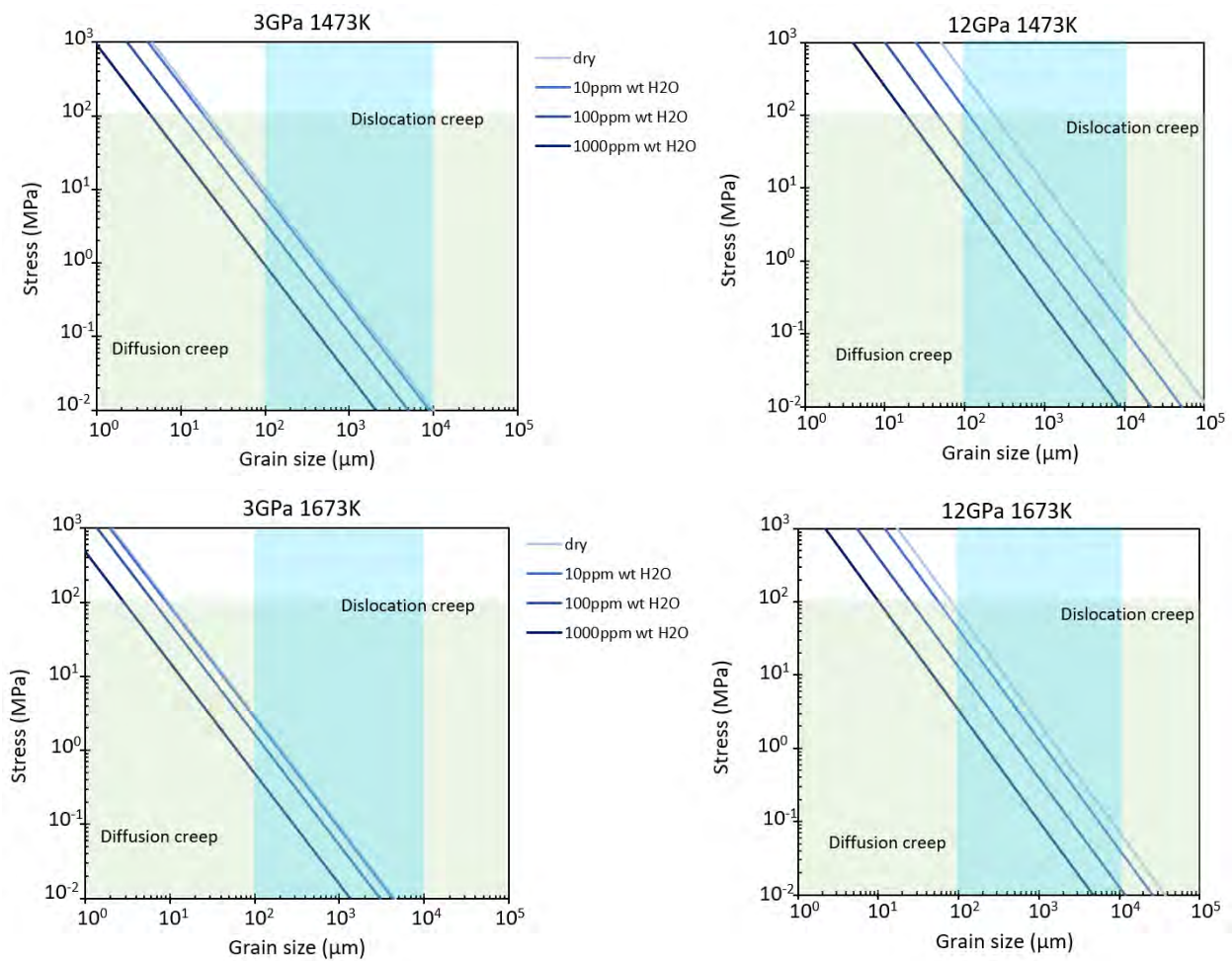723 and the green region represents the stress range expected in the upper mantle.

724

725
726
727
728

729 **List of Tables**

730 **Table 1:** Experimental conditions for each run and grain sizes for San Carlos and solgel samples.

731 *The value of strain rate was determined on the Stress-Strain plot at the last point where

732 diffusion creep operated (see Section 3.3).

Deformation run	P (GPa)	T (K)	Sample	Initial grain size (μm)	Final grain size (μm)
SAN 536	2.9± 0.3	1065 ± 33	San Carlos (K2090)	0.23 (0.15)	0.30 (0.24)
			Solgel (K2091)	0.18 (0.12)	0.23 (0.15)
SAN 513	4.7 ± 0.9	980 ± 110	San Carlos (K1980)	0.17 (0.11)	0.18 (0.12)
			Solgel (K2034)	0.17 (0.11)	0.17 (0.11)
SAN 515	5.9 ± 0.2	1080 ± 90	San Carlos (K2036)	0.21 (0.14)	0.78 (0.53)
			Solgel (K2034)	0.17 (0.11)	0.53 (0.36)
SAN 514	8.8 ± 0.3	1249 ± 47	San Carlos (K1984)	0.39 (0.27)	0.98 (0.67)
			Solgel (k1976)	0.38 (0.26)	0.98 (67)

733

734

735

736 **Table 2:** The mechanical data for diffusion creep used in the activation volume calculation. The
737 stress value* and strain rate** were obtained from the point on time evolving stress/strain curve
738 where diffusion creep is still operational before transition. The calculated grain size***
739 corresponds to time coordinate where stress and strain values were selected (see the main text for
740 expanded discussion).

Deformation run	Sample	Stress* (MPa)	Strain rate** x 10^{-6} (s^{-1})	Calculated grain size*** (µm)
SAN 536	San Carlos (K2090)	110 ± 25	4.21 ± 0.21	0.24 (0.20)
	Solgel (K2091)	55 ± 27	2.32 ± 0.12	0.18 (0.15)
SAN 513	San Carlos (K1980)	250 ± 21	0.49 ± 0.003	0.17 (0.12)
	Solgel (K2034)	100 ± 13	0.2 ± 0.01	0.15 (0.10)
SAN 515	San Carlos (K2036)	510 ± 30	2.62 ± 0.17	0.35 (0.23)
	Solgel (K2034)	400 ± 16	1.74 ± 0.87	0.26 (0.17)
SAN 514	San Carlos (K1984)	950 ± 55	9.52 ± 0.48	0.63 (0.42)
	Solgel (k1976)	940 ± 60	8.49 ± 0.42	0.62 (0.42)

741

742

743

744 **Table 3:** Activation volume and pre-exponential factor A (s^{-1} MPa^{-n} μm^{m}) for different stress

745 exponents and different activation energies. A and error in A are reported in log base 10.

746

San Carlos								
Normalization parameters					Calculated A and V*			
E* (kJ/mol)	m	T (K)	d (μm)	Stress (MPa)	log (A)	Error in log (A)	V* (cm³/mol)	Error in V* (cm³/mol)
295	2	1100	1	50	6.56E+00	6.43E+00	**6.90E+00**	9.00E-01
295	3	1100	1	50	5.42E+00	4.89E+00	**5.20E+00**	4.00E-01
375	2	1100	1	50	1.11E+01	1.16E+01	**9.40E+00**	2.30E+00
375	3	1100	1	50	9.93E+00	1.02E+01	**7.70E+00**	1.60E+00
Solgel								
Normalization parameters					Calculated A and V*			
E* (kJ/mol)	m	T (K)	d (μm)	Stress (MPa)	log (A)	Error in log (A)	V* (cm³/mol)	Error in V* (cm³/mol)
295	2	1100	1	50	6.27E+00	6.18E+00	**6.50E+00**	9.00E-01
295	3	1100	1	50	4.94E+00	4.49E+00	**4.40E+00**	5.00E-01
375	2	1100	1	50	1.08E+01	1.13E+01	**9.00E+00**	2.30E+00
375	3	1100	1	50	9.45E+00	9.73E+00	**6.90E+00**	1.60E+00

747

748